The role of vast off-stoichiometry of SnSe thin film on structural, morphological, optical, and electrical properties for photovoltaic applications

Prosenjit Sarkar[1], Nisha[1], Pawan Kumar[1,*] (ID), and Ram S. Katiyar[2]

[1] *Department of Physics, Gurukula Kangri (Deemed to Be University), Haridwar 249404, India*
[2] *Department of Physics, University of Puerto Rico, San Juan, PR 00931, USA*

ABSTRACT

A layered chalcogenide material, tin monoselenide (SnSe), has recently garnered considerable interest in optoelectronics owing to its remarkable opto-electrical properties. Our goal in conducting this research is to better understand the SnSe vast off-stoichiometry ratio. The structural properties of all films examined by X-ray diffraction (XRD) confirmed formation of orthorhombic SnSe with a prominent (111) orientation peak. Raman spectroscopy revealed the successful formation of a single phase of α-SnSe under Sn-rich conditions. The calculated direct bandgap using Tauc's plot is found to be increased from 1.37 eV (under Sn rich) to 1.68 eV (under Se-rich). Based on Hall measurement, largest carrier mobility (34.3 $cm^2V^{-1}S^{-1}$) is found in Sn-rich SnSe conditions. The results show how off-stoichiometry-related imperfections have a significant impact on opto-electrical characteristics. And by adjusting the Sn/Se ratio, the conductivity type can be modified. Using this approach will undoubtedly result in an improvement in the overall performance of thin-film solar cells. This will enable the fabrication of extremely efficient SnSe homojunction solar cells.

1 Introduction

A layered chalcogenide material, has recently garnered considerable interest in optoelectronics owing to its layered-dependent opto-electrical properties [1]. As members of the layered chalcogenide material family, the binary tin chalcogenides, which belong to IV–VI group family, are promising materials for optoelectric and thermoelectric applications because of their low cost, lower toxicity, earth abundance, and

tunable bandgap properties [2]. Over the last few years, several laboratories have concentrated on tin chalcogenide materials such as tin selenide (SnSe). The lattice parameters of SnSe are a = 11.4976 Å, b = 4.1533 Å, and c = 4.44 Å at room temperature, making it an orthorhombic crystal structure [JCPDS no. 00-048-1224]. Tin selenide is a desirable material for use in optoelectronic applications due to its optimal optical bandgap value (1.0–1.5 eV), strong absorption coefficient (up to 10^5 cm^{-1}), and predicted

Springer

efficiency of 32% [2–5]. As a result, there is a strong possibility that this material will replace hazardous (Cd-based) and multielement-based materials like CIGS (copper indium gallium selenide) and CZTS (copper zinc tin sulfide) photovoltaic absorbers. However, SnSe-based solar cells currently exhibit less efficiency (in both vacuum and non-vacuum environments) as compared to the above-mentioned material-based solar cells [6]. Reduced efficiency is primarily due to non-ideal band alignment at heterojunction interfaces, back-and-front-electrode recombination, bulk defects, and secondary phases, along with SnSe [7].

Different deposition techniques are used to deposit SnSe thin films, such as thermal evaporation [8], chemical vapor deposition [9], electrodeposition [10], spray pyrolysis [11], and magnetron sputtering [12]. Deposition techniques significantly influence the properties of the films, like optical bandgap, crystallographic orientation, surface roughness, porosity, elemental composition, and electrical conductivity. The thermal evaporator is one of the technologies that is most frequently used to deposit thin films for a wide variety of applications due to its cost-effectiveness, ease of use, and low contamination during deposition [13].

The ability to manipulate the carrier type in SnSe is quite advantageous for fabricating SnSe-based homojunction solar cells. Based on the literature review of n-type SnSe, we found that the majority of n-type is produced through the process of doping; however, the electrical properties of this type of SnSe are still unsatisfactory due to low carrier concentrations or mobility [14–16]. In contrast, doping SnSe with donor or acceptor elements is significantly more difficult than doping other IV–VI chalcogenide semiconductors, such as PbTe or GeTe. It is therefore quite difficult to tune the n-type charge carrier in SnSe to an optimal level due to intrinsic p-type conductivity of the material.

To our knowledge, few recent research works (other than reviews) report the off-stoichiometry effect on the physical properties of SnSe thin film for thermoelectrical properties [17]. However, no one addresses the optoelectrical properties of the vast off-stoichiometric ratio for controlling the physical parameters of SnSe. This work presents a comprehensive report on the morphological, microstructural, optical, and electrical characteristics of SnSe thin films with widely varying off-stoichiometry. The main goal of this research is to modify the optical bandgap and conductivity by changing the ratio of Sn to Se.

2 Experimental

2.1 Synthesis

Tin monoselenide has traditionally been synthesized by either precipitating it from aqueous solutions or synthesizing it through elemental combination at higher temperatures. But these processes either require a lot of energy or toxic chemicals [4]. In this process, only the primary elements Tin (Sn) powder (Nanografi, 99.95%) and Selenium powder (SRL, 99.999%) are used to synthesize pure Tin monoselenide (SnSe). The different stoichiometry ratios (3:2), (1:1), and (2:3) of Sn and Se are mechanically crushed for 30 min with a mortar and pestle. In an open air-muffle furnace, one gram of mechanically ground mixture is kept in a covered silica crucible (25 ml) and heated at a very slow rate of 1 °C per minute. The optimal reaction temperature, which is higher than the melting points of tin and selenium, was 350 °C. It naturally cooled down after being kept at a constant temperature of 350 °C for two hours. The cooled SnSe crystals are mechanically ground again for 30 min using a mortar and pestle to reduce particle size.

2.2 Thin film deposition

SnSe thin-film layer was deposited using a single-source thermal evaporation technique. Microscopically small glass substrates were used in this work with the intention of characterizing the substance of the deposited thin films. To obtain a chemically cleansed glass surface prior to deposition, a traditional cleaning technique using acetone, methanol, Labolene solutions, and distilled water was used. The glass surface was then dried on a blower for 30 min. 40 Amps of constant current were utilized to evaporate synthesized SnSe nanoparticles from a molybdenum boat. SnSe thin film was deposited for 30 min at a modest deposition rate of approximately 5 Å / sec and a vacuum pressure of greater than 10^{-4} mbar. The substrates were placed at 14-cm vertical distance from the source. The process used for synthesized and deposition techniques is depicted graphically

(see Fig. 1). $Sn_{60}Se_{40}$, $Sn_{50}Se_{50}$, and $Sn_{40}Se_{60}$ thin films are deposited by utilizing synthesized nanoparticles at (3:2), (1:1), and (2:3) stoichiometry ratios, respectively. A stylus profiler determined the film's thickness to be around 889 ± 10 nm.

2.3 Characterization

Morphological and elemental studies of all samples were done by scanning electron microscope (SEM) (model: Zeiss Auriga FIB-SEM system coupled with an elementary detector). The microstructural properties of the deposited thin films were studied by XRD using a Cu-Kα radiation source (model: PANalytical X-pert Pro). To further confirm the phase purity, Raman spectroscopy (model: Confocal Raman Spectrometer with PL) was used. Absorption spectra of all thin films have been recorded by UV–Vis-NIR spectrophotometer (model: Shimadzu—3600). Metal contact is made on all thin films by for electrical measurement by using Ag metallic paste. Under normal conditions, Current–Voltage (I–V) characteristics were measured by Keithley source-meter 4200. Hall measurement system (model: HMS-5000 series/ HMS-7000 series), using 5 mA current and $\pm$ 0.55 T magnetic field, was used to know about the current transport properties.

3 Result and discussion

3.1 Elemental composition of prepared powder

SEM with Energy-dispersive X-ray spectroscopy (EDS) was utilized to observe the morphology and elemental content of all synthesized nanoparticles produced by a temperature-assisted mechanochemical process. Using point analysis, the SEM images and elemental composition of each sample was determined. Figure 2 shows the captured SEM images with elemental reports. Only Sn and Se are seen in Fig. 2, highlighting the purity of the synthesized product. The EDS did not find any further oxides containing tin. The reported weight and atomic percentage of the constituents are listed in the inset table in Fig. 2. $Sn_{50}Se_{50}$ demonstrates a Sn-enriched SnSe phase with a Sn/Se ratio of 1.11, which is nearly the stoichiometric ratio of typical SnSe material. The actual Sn/Se ratio is slightly higher than it was before the synthesis because selenium ions were lost during the method due to volatilization in the open air.

3.2 Structural analysis

The phase structure of the thin films was investigated by XRD techniques. Figure 3a depicts the diffraction pattern of SnSe thin films of different stoichiometry. All the observed XRD peaks are attributed to the orthorhombic SnSe (JCPDS Card No. 00-48-1224) with the P_{nma} space group. In the XRD pattern of a thin film of $Sn_{60}Se_{40}$, a relatively sharp peak is
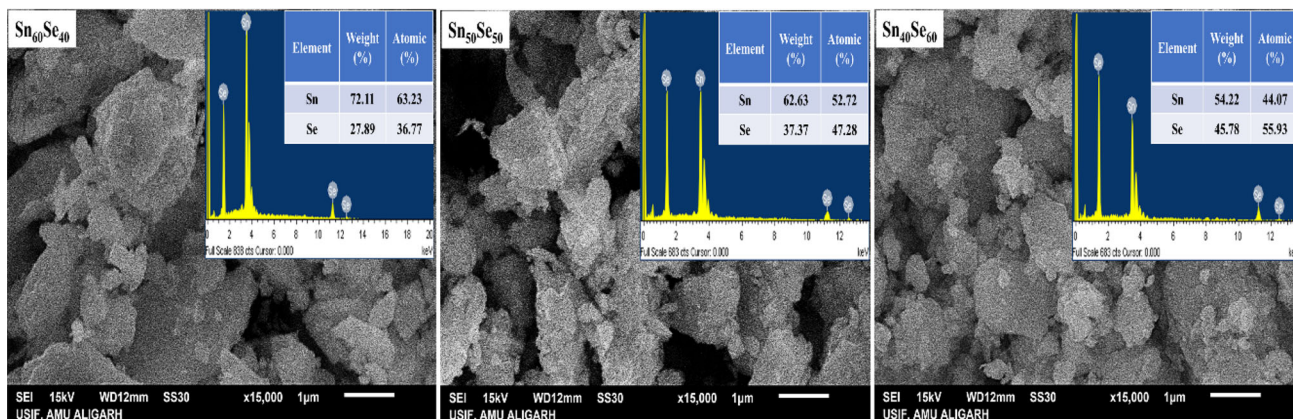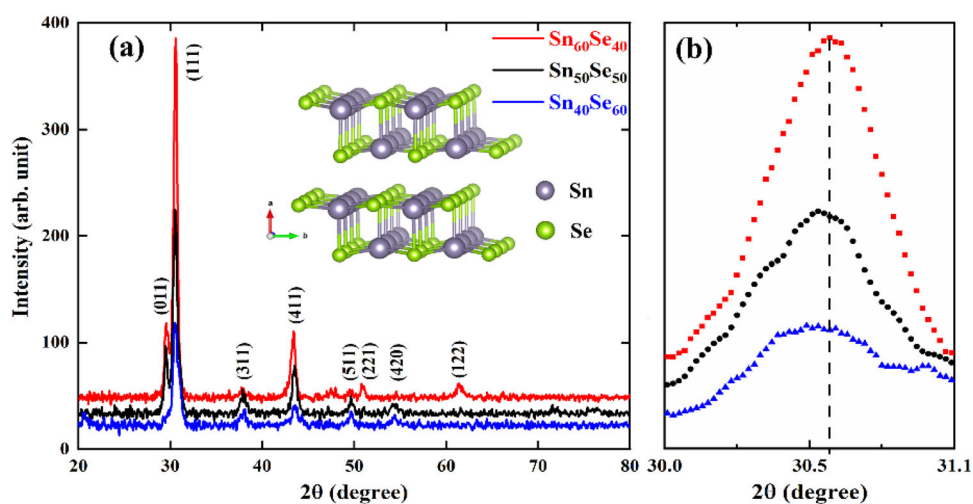

Fig. 1 Schematic diagram of experimental process
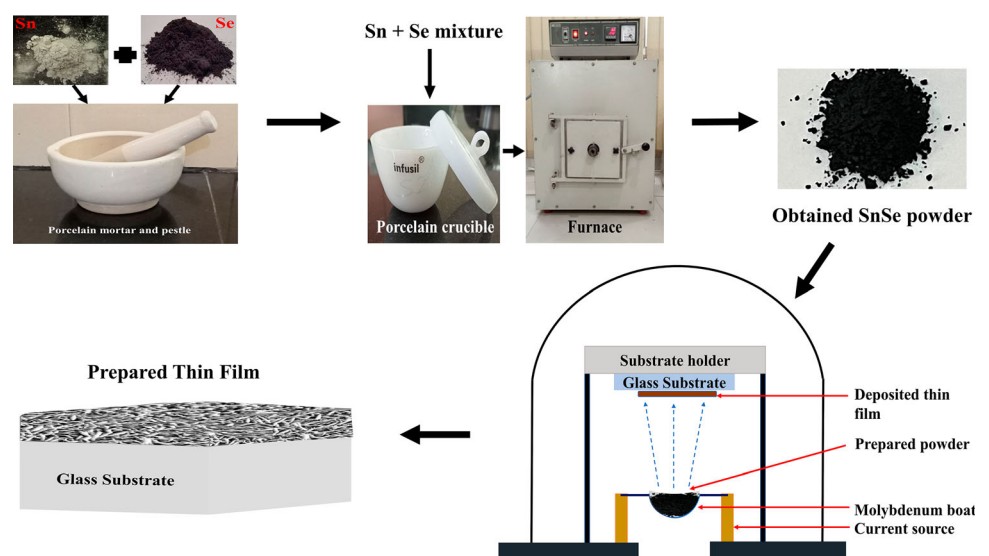
Fig. 2 Compositional report of all SnSe thin films

Fig. 3 XRD pattern of (**a**) all SnSe thin films and crystal structure of orthorhombic SnSe (**b**) enlarge view of (111) peak

detected due to the larger crystallite size. In all XRD patterns, regardless of non-stoichiometry, the (111) diffraction peak is the dominant peak. The predominant (111) peak boosts the solar cell's efficiency [18]. The non-stoichiometry is strongly influenced by the strength and shift of the (111) peak. A magnified view of (111) peak in Fig. 3b reveals that (111) peak of Se-rich SnSe is shifted to the lower angle side compared to Sn-rich SnSe. The Sn phase (JCPDS Card No. 00-04-0673) is not visible in the XRD results for films produced under Sn-rich conditions, as indicated by EDX. This provides evidence that some of the excess tin that was present in the SnSe crystal has been incorporated into the structure of the crystal lattice. The highest [Se/Sn] ratio films would most likely have contained the $SnSe_2$ phase (JCPDS Card No. 00-23-0602). According to previous research [19], the SnSe film compensates for an increase in selenium content by producing more Sn vacancies, which causes a change in oxidation state of Sn from + 2 to + 4. This would increase the potential for the formation of the $SnSe_2$ phase impurity, which have many oxidation states for Sn. The $SnSe_2$ phase is not present in Se-rich films, as shown in the phase diagram.

Additionally, the intensities of the (011) and (411) peaks for SnSe rose as the Sn concentration increased. In addition, for films with a high Sn content, the peaks (311), (511), and (420) have nearly disappeared, while new peaks (031), (122), and (221) have appeared. In excess Se-content film, the strength of all peaks is diminished relative to $Sn_{50}Se_{50}$ thin film, and the (011) peak at an angle of around 29.5° has nearly disappeared. To study the crystallinity of all off-stoichiometry thin films, the average crystallite size is calculated using the relation [20],

$$D = \frac{k\lambda}{\beta \cos\theta}$$

as well as strain formula [21],

$$\varepsilon = \frac{\beta \cot\theta}{4}$$

in which $k = 0.9$ is shape factor, λ is the employed X-ray wavelength (1.54 Å) of Cu-K$_\alpha$ radiation, β represents the full width at half maximum (FWHM) of the diffracted peak, and θ is the Bragg's angle. The average crystallite size and micro-strain of the planes for Sn-rich SnSe orthorhombic phase are 21 nm and 5.40×10^{-3}, respectively. As the [Sn]/[Se] ratio fluctuated from 1.50 to 0.50, the crystallite size fell from 21 to 13 nm. This increase in crystallite size is due to the improvement in crystallinity caused by an increase in the tin/selenium ratio. The unit cell lattice parameters and interatomic distance between Sn and Se are also computed using Rietveld refinement analysis using the XRD peak positions. The effect of vast off-stoichiometry on SnSe lattice structure is displayed in Fig. 4. The refined lattice parameters of $Sn_{50}Se_{50}$ are $a = 11.48$ Å, $b = 4.13$ Å, $c = 4.38$ Å, and $\alpha = \beta = \gamma = 90°$, which are in close match with the previous reported values: $a = 11.50$ Å, $b = 4.15$ Å, $c = 4.44$ Å, and $\alpha = \beta = \gamma = 90°$ of orthorhombic SnSe (inset Fig. 3a). All the samples contained a smaller unit cell volume than the standard value (212.02 $\times 10^6 pm^3$). It may be due to off-stoichiometry or an amorphous substrate.

The deformation of the unit cell was observed as the Sn-concentration in SnSe crystals increased, despite the small range of the Sn/Se atomic ratio [22]. As the Sn-content rises, the lattice parameters 'a' and 'b' expand, while parameter 'c' contracts. This pattern of relaxation complements its unique, layered structure perfectly. The lattice parameter 'b' is essentially

fixed within the cleavage a–b plane, whereas the parameter 'a' changes slightly as Se-content increases. Table 1 lists all of the computed values for the microstructure parameters.

Using the standard JCPDS, we can see that the highly intense peaks of the $SnSe_2$, α-SnSe, and Sn phases all fall within the limited range of diffraction angle, 30.4–30.7° ($2\theta = 0.3°$). Therefore, it is challenging to determine the formation of the pure α-SnSe phase based merely on the XRD pattern. However, other phases may be present at concentrations below the detection range of XRD (2 wt% of the sample). Therefore, Raman spectroscopy was used to examine the deposited films and determine the purity of the phase.

3.3 Raman analysis

According to XRD analyses, all of the samples are in crystalline phases. It's possible that other secondary phases exist in small proportion but can't be seen using XRD technology. All samples are acquired for Raman spectroscopy in order to conduct thorough analyses. Figure 5a depicts the room-temperature Raman scattering data of all thin films using a laser excitation wavelength of 532 nm. The peak intensity of the $Sn_{60}Se_{40}$ sample is greater than that of the $Sn_{40}Se_{60}$ sample, as can be seen in Fig. 5. Moreover, some clearly defined peaks and some broader peaks can be found in the Raman spectra of each sample. Therefore, all broad peaks are deconvolved for in-depth analysis. Following background subtraction, the gaussian deconvoluted Raman spectra of each sample are displayed in Fig. 5b–d.

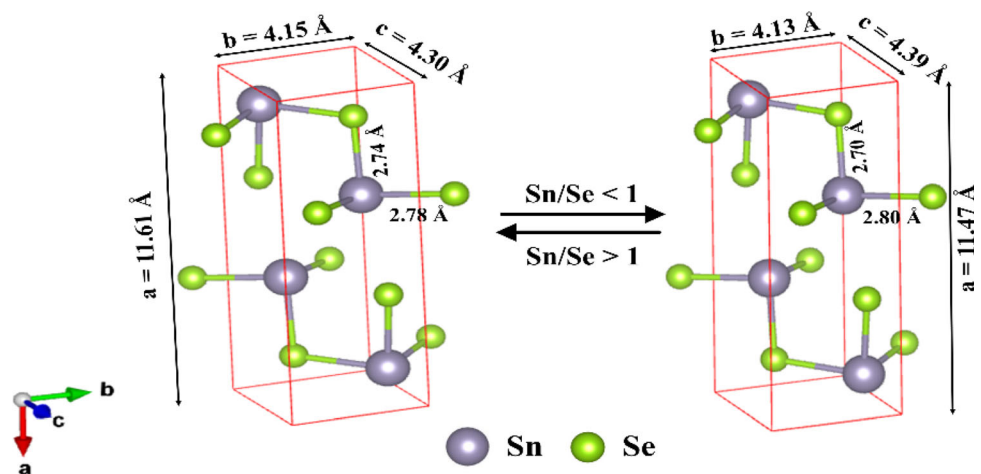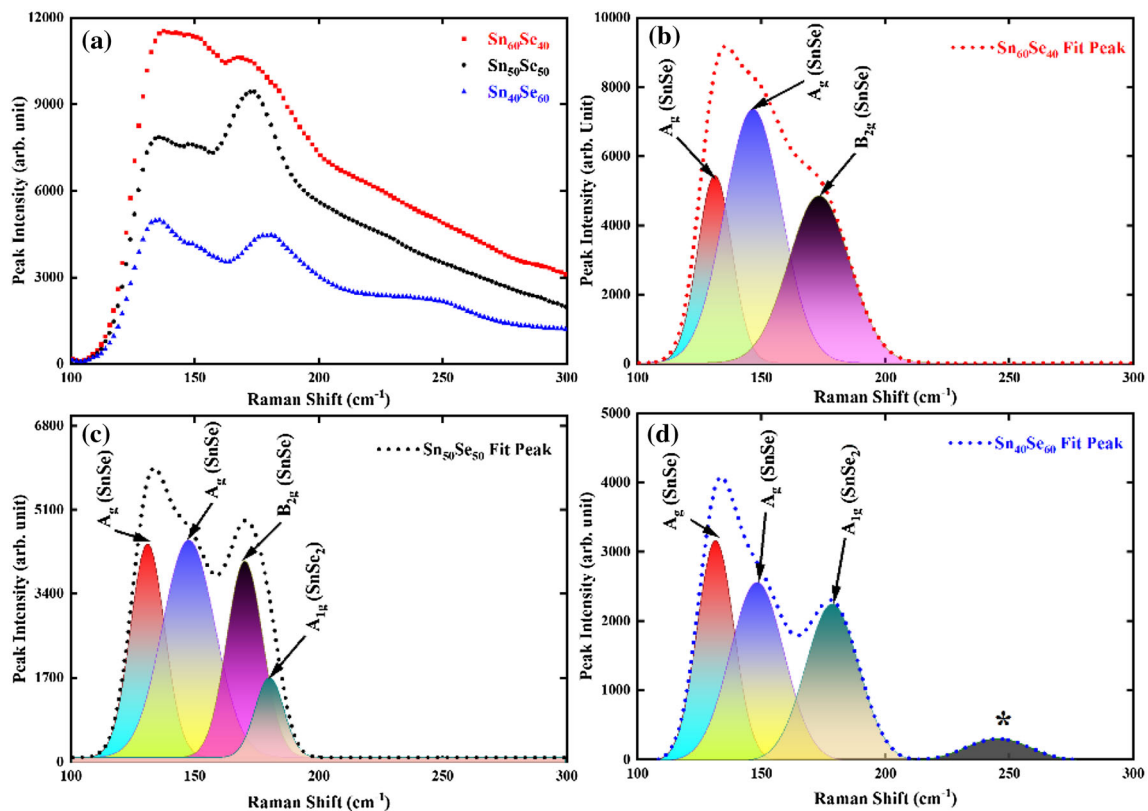**Fig. 4** Effect of excess Sn and Se on SnSe lattice structure

Table 1 Microstructural parameters of all SnSe thin films

Sample	$Sn_{60}Se_{40}$	$Sn_{50}Se_{50}$	$Sn_{40}Se_{60}$
Avg. crystallite size (nm)	21	17	13
Avg. micro-strain ($\varepsilon \times 10^{-3}$)	4.57	6.79	9.06
Lattice parameters (Å)	$a = 11.61$ (1)	$a = 11.48$ (9)	$a = 11.47$ (1)
	$b = 4.15$ (4)	$b = 4.13$ (3)	$b = 4.13$ (4)
	$c = 4.30$ (6)	$c = 4.38$ (4)	$c = 4.39$ (6)
Cell volume (10^6 pm^3)	207.20	207.84	208.18

Fig. 5 (a) Raman spectra of all samples; deconvolution of Raman spectra peaks of (b) $Sn_{60}Se_{40}$ (c) $Sn_{50}Se_{50}$ (d) $Sn_{40}Se_{60}$ thin film

The Raman spectra of $Sn_{50}Se_{50}$ samples exhibit four significant peaks at 131, 146, 170, and 180 cm^{-1}. The observed peaks at 131 and 146 cm^{-1} have both been attributed to the A_g mode of the SnSe layer [23, 24]. Two bands with peak maxima at 170 cm^{-1} (B_{2g} mode of SnSe layer) and 180 cm^{-1} (A_{1g} mode of SnSe$_2$ layer) combine to form a sharp and highly intense peak maximum at 174 cm^{-1} (see Fig. 5c) [25]. As shown in Fig. 5, high-intense peaks at 174 cm^{-1} shifted toward a lower wavenumber as the tin-content increased. The presence of SnSe$_2$ peaks has completely disappeared. The single-phase SnSe formation is confirmed by the analysis of Raman spectra of $Sn_{60}Se_{40}$ thin film (131, 146, and 169 cm^{-1}), as

shown in Fig. 5b. The film grown at excess selenium contents showed a clearly shifted peak of 174 to 179 cm^{-1} toward SnSe$_2$. This suggests that there is a clear presence of the SnSe$_2$ impurity phase at higher selenium contents, although the XRD analysis does not find any evidence of its existence. In addition to these peaks, the selenium-rich sample displays a small shoulder at approximately 238 cm^{-1} indicated by a star (*) (see Fig. 5d). This characteristic corresponds to a trigonal Se structure, according to previous research [26]. The results of XRD patterns show that the variations in the Raman band intensity are frequently related to variations in the crystalline quality of semiconducting nanostructures. Raman

analysis proposed that $Sn_{50}Se_{50}$ and $Sn_{40}Se_{60}$ thin films are not single-crystalline, having mixture phases of Se, SnSe, and $SnSe_2$, while $Sn_{60}Se_{40}$ thin film is pure single-crystalline.

3.4 Morphological studies

The influence of vast off-stoichiometry on the morphology of α-SnSe films was studied by SEM. Figure 6 shows the surface morphology of the deposited thin films using different Sn:Se ratios. The SEM images revealed that all the films were well covered on the glass substrate with uniform grain sizes. The difference in morphology is clearly observed by SEM images. In Sn-rich films, the flakes-shaped grains have a vertical growth in the direction of the a-axis, as compared to that of $Sn_{50}Se_{50}$. As the selenium concentration increases, the grain size is broken into smaller grains with high packing and uniformity. The optical properties of nanostructures can be drastically altered due to the increase in surface area brought about by the uniform and dense packing of the grains. According to XRD analysis, the intensity of (011) peak is diminished in Se-rich SnSe thin film, while the intensity of the remaining peak is decreased. Consequently, as the Se-content increases, the crystallite size reduces, resulting in the formation of relatively small grains, as depicted in Fig. 6. Thus, it can be concluded that XRD patterns and SEM images are intrinsically linked to one another.

3.5 Optical studies

To figure out the impact of off-stoichiometry on the optical properties, room-temperature UV–vis spectroscopy was used as an analytical tool. Measurements of optical absorption were performed in the region of 300–2000 nm to calculate the absorption coefficient and optical band gap. Figure 7a depicts the dependence of absorbance on wavelength for various stoichiometric circumstances in all SnSe films. Absorption spectra reveal that Sn-rich thin films are well-suited for use in solar cells due to their high absorption value across a wide spectral range (300–800 nm). Se-rich SnSe thin film absorbs less light in the visible range than Sn-rich SnSe thin film.

Based on the absorbance values, the absorption coefficient (α) of all thin films is calculated by the Lambert–Beer relation [27] below:

$$\alpha = \frac{2.303 \times A}{t}$$

where t is the thickness of thin film and, A is the absorbance of SnSe thin film. The evaluated absorption coefficient is shown in the inset of Fig. 7a. In the visible region, all thin films are found to have a higher absorption coefficient ($> 10^4$ cm^{-1}), positioning them on a scale with other good photovoltaic materials [28].

To determine the absorption edge, the optical energy band gap E_g needs to be determined. The energy gap, E_g can be obtained as follow [29]:
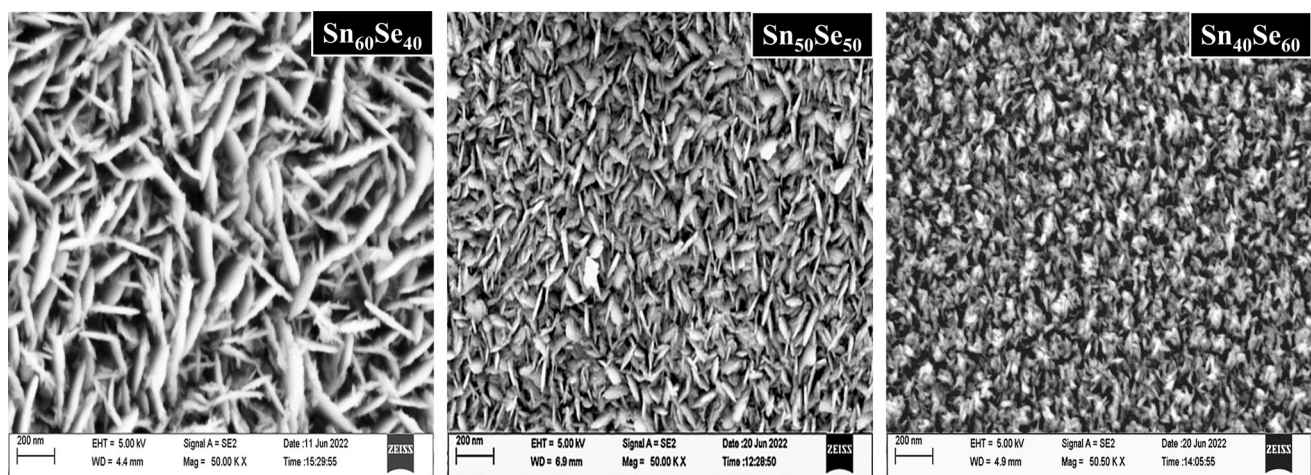
$$(\alpha h v)^n = A(h v - E_g)$$

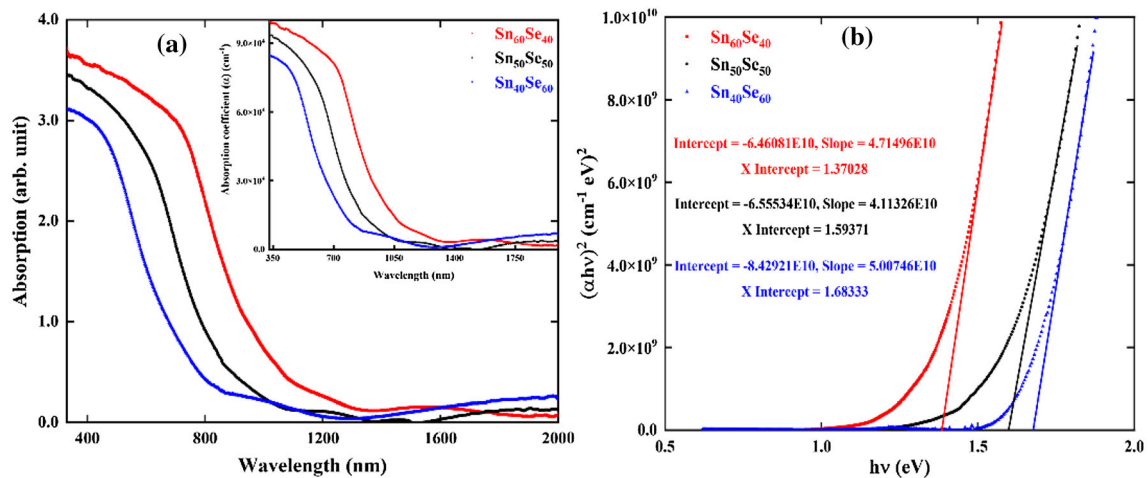

Fig. 6 SEM images of all SnSe thin films

Fig. 7 (**a**) Absorption spectra and absorption coefficient (inset) of all SnSe thin film; (**b**) Direct optical bandgap of all SnSe thin film by Tauc plot

where n describes the transition process, hv is the photon energy of incident ray, A is a constant, and E_g is band gap of material. For direct allowed and forbidden transitions, n has values of 2 or 2/3, respectively, but for indirect allowed and forbidden transitions, n has values of 1/2 and 1/3. Figure 7b depicts a typical Tauc's plot used to estimate the direct band gap for SnSe thin film at different off-stoichiometry.

The estimated direct band gap from the intercept of plot $(\alpha hv)^2$ and hv is 1.37, 1.59, and 1.68 eV for $Sn_{60}Se_{40}$, $Sn_{50}Se_{50}$, and $Sn_{40}Se_{60}$, respectively. The strong influence of off-stoichiometry is clearly observed in optical analyses. The previous reported direct band gap energy of SnSe thin film varied between 0.9 and 1.8 eV [7, 30]. Based on the literature data, the band gap is significantly affected by crystallite size and the presence of other tin selenide phases like $SnSe_2$ [31]. The results of the XRD and Raman spectroscopy, as well as the lower E_g values, rule out the presence of any other tin phases in the Sn-rich sample. This research suggests that a larger crystallite size caused by a high Sn/Se value would result in a lower E_g value. Due to the presence of $SnSe_2$ in the sample, the optical band gap shifts systematically toward a larger band gap. As a result, the optical band gap value of a particular composite can be engineered to have the desired value by adjusting the relative ratios.

3.6 Hall measurement

The Van der Pauw method was used to measure the Hall effects to find out what caused the electrical conductivity. The relationship between the stoichiometry ratio and the variations in the conductivity, carrier concentration, and Hall mobility of the films is represented graphically in Fig. 8. A reduction in hall conductivity (30 Ω^{-1} cm^{-1} to 9.4 Ω^{-1} cm^{-1}) and Hall mobility (34.3 to 21.2 cm^2 V^{-1} s^{-1}) is visible along with the rise in the stoichiometric ratio. Therefore, we postulated that the bonding environment surrounding Sn atoms might be altered by excess Sn-induced defects (antisites, interlayers/interstitials Sn, Se vacancies) [22]. The results indicate that Se-rich SnSe thin films are more resistant than Sn-rich SnSe thin films. As shown in Fig. 5d, in Raman analysis of Se-rich SnSe samples, other tin phases such as $SnSe_2$ are found. According to
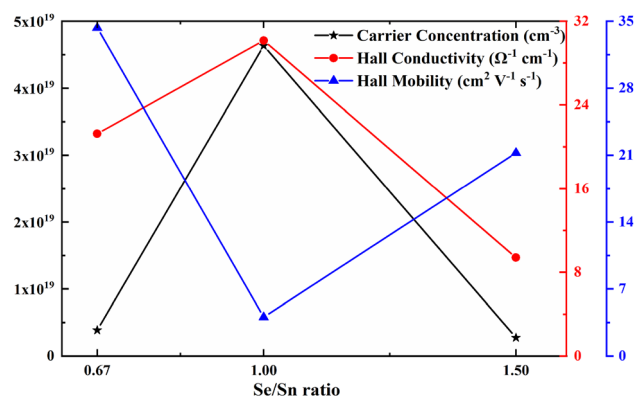

Fig. 8 Recorded Hall parameters of all SnSe thin films

previous studies, secondary phases have an impact on the electrical properties of the film; the n-type nature of $SnSe_2$ would cause the selenium-rich SnSe to have a higher resistivity [28]. Based on the hall measurement, $Sn_{60}Se_{40}$ or $Sn_{50}Se_{50}$ films show n-type behavior, whereas the $Sn_{40}Se_{60}$ film exhibits p-type behavior. There are six different native point defects in the tin-sulfur system, including vacancies (V_{Sn}, V_S), interstitials (Sn_i, S_i), and antisite defects (Sn_S, S_{Sn}). Vacancies may be regarded as localized acceptor and donor states. Since the investigated films were transformed from Sn-rich to S-rich, the probability of V_{Sn} formation should be quite high [32]. Due to chemical similarities between SnS and SnSe, Se-rich SnSe thin films are expected to have p-type conductivity and V_{Sn} as the main acceptor.

Based on XRD analysis, large crystallite sizes are found in Sn-rich SnSe thin film, which causes a decrease in the electrical resistivity and then high mobility. The conversion efficiency of solar cells can be increased by employing materials with high carrier mobility. Therefore, it is possible that the SnSe film, due to its higher carrier mobility and lower resistivity, is better suited for use in photovoltaic devices. This analysis demonstrates that optimizing the stoichiometry of SnSe is crucial for achieving the desired electrical properties.

3.7 Current–voltage characterization

Figure 9 depicts the current–voltage (I–V) plot under normal illumination using two probe method for all the samples with different stoichiometry. All of the
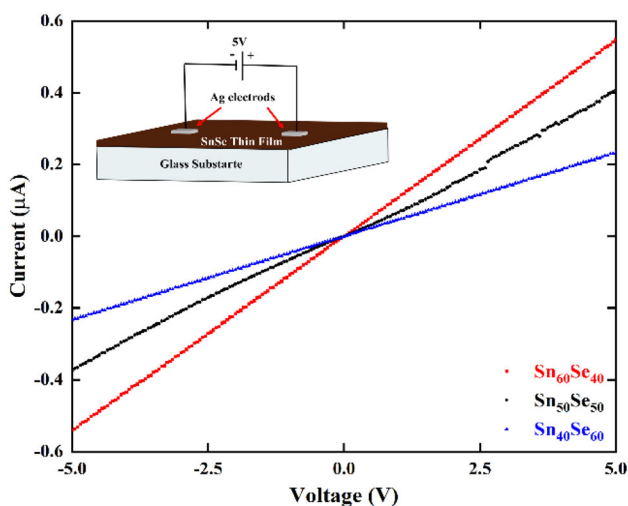

Fig. 9 Current–Voltage characteristics of all SnSe thin films

samples display a curve that is linear and symmetrical, which suggests that ohmic contact characteristics exist between the thin films and Ag metal contact. The off-stoichiometry has a substantial impact on the I–V characteristics, as depicted in Fig. 9. When the ratio of Sn/Se is greater than 1 $Sn_{60}Se_{40}$ thin film exhibits the highest current (0.55 µA) at 5 V. On the other hand, the current of $Sn_{40}Se_{60}$ thin film when Sn/Se is lower than 1 is approximately 0.23 µA. The results show that, compared to SnSe thin films, Se-rich SnSe is more resistive and Sn-rich SnSe is more conductive. The crystal size and stoichiometry ratio of the film both have an effect on its electrical conductivity.

4 Conclusion

The outcomes of this investigation demonstrated the impact of Sn/Se ratio on microstructural and opto-electric properties of SnSe films. The approach aims to synthesize off-stoichiometry SnSe using a less expensive temperature-assist mechanochemical process, which is subsequently deposited onto a glass substrate using a thermal evaporator. XRD and Raman analyses reveal the enriched Sn-content to be in the form of pure orthorhombic SnSe with a dominant (111) reflection peak. However, enrichment of the Se content reveals the mixed phase of SnSe and other tin phases. According to the SEM images, films thoroughly cover the entire substrate, and differences in morphology may be clearly seen. When Sn-rich SnSe is transformed into Se-rich SnSe, the direct band gap shifts from 1.37 eV to 1.68 eV, and the conductivity changes from n to p-type. Consequently, altering the ratio of Sn to Se can help optimize the band gap, electrical conductivity, and carrier mobility. This technique for fabricating n-type SnSe thin films will undoubtedly be essential for enabling SnSe homojunction solar cells.

Author contributions

Study conception and design contributed by all authors. Material preparation, data collection and analysis were performed by N and PS. The first draft of the manuscript was written by N and all authors commented on previous versions of the manuscript. All authors read and approved the final manuscript.

Data availability

The data sets generated during and/or analyzed during the current studies are available from the corresponding author on reasonable request.

Declarations

Conflict of interest   The authors declare that they have no known competing financial interests or personal relationships that could have appeared to influence the work reported in this paper.

References

1.   J. Singh, S. Kumar, R.K. Soni, J. Alloys Compd. **849**, 156502 (2020)
2.   V.R. Minnam Reddy, S. Gedi, B. Pejjai, C. Park, J. Mater. Sci. Mater. Electron. **27**, 5491 (2016)
3.   W. Shi, M. Gao, J. Wei, J. Gao, C. Fan, E. Ashalley, H. Li, Z. Wang, Adv. Sci. **5**, 1700602 (2018)
4.   R. Indirajith, T.P. Srinivasan, K. Ramamurthi, R. Gopalakrishnan, Curr. Appl. Phys. **10**, 1402 (2010)
5.   Z. Li, Y. Guo, F. Zhao, C. Nie, J. Shi, X. Liu, S. Zuo, J. Jiang, Vacuum **177**, 109343 (2020)
6.   P. Beltrán-Bobadilla, A. Carrillo-Osuna, J. A. Rodriguez-Valverde, B. Acevedo-Juárez, I. Montoya De Los Santos, F. J. Sánchez-Rodriguez, A. Maykel Courel, P. Beltrán-Bobadilla, A. Carrillo-Osuna, J. A. Rodriguez-Valverde, B. Acevedo-Juárez, I. Montoya De Los Santos, F. J. Sánchez-Rodriguez, and A. Maykel Courel, Gen. Chem. **7**, 200012 (2021).
7.   M. Kumar, S. Rani, Y. Singh, K.S. Gour, V.N. Singh, RSC Adv. **11**, 6477 (2021)
8.   M.R. Burton, T. Liu, J. McGettrick, S. Mehraban, J. Baker, A. Pockett, T. Watson, O. Fenwick, M.J. Carnie, Adv. Mater. **30**, 1801357 (2018)
9.   Y. Feng, X. Zhang, L. Lei, Y. Nie, G. Xiang, RSC Adv. **10**, 11990 (2020)
10.   N.R. Mathews, Sol. Energy **86**, 1010 (2012)
11.   S. Anwar, S. Gowthamaraju, B.K. Mishra, S.K. Singh, S. Anwar, Mater. Chem. Phys. **153**, 236 (2015)
12.   L. Song, J. Zhang, B.B. Iversen, J. Mater. Chem. A **7**, 17981 (2019)
13.   E. Coskun, H.H. Gullu, C. Emir, M. Parlak, Phys. B Condens. Matter **604**, 412669 (2021)
14.   T. Shen, K.Y. Li, Z.J. Chen, H.F. Wu, J.X. Si, J. Electron. Mater. **49**, 621 (2020)
15.   T. Horide, K. Nakamura, Y. Hirayama, K. Morishita, M. Ishimaru, K. Matsumoto, A.C.S. Appl, Energy Mater. **4**, 9563 (2021)
16.   C. Chang, Q. Tan, Y. Pei, Y. Xiao, X. Zhang, Y.X. Chen, L. Zheng, S. Gong, J.F. Li, J. He, L.D. Zhao, RSC Adv. **6**, 98216 (2016)
17.   W. Ting Wang, Z. Hao Zheng, F. Li, C. Li, P. Fan, J. Ting Luo, B. Li, J. Alloys Compd. **763**, 960 (2018)
18.   Z. Li, Y. Guo, F. Zhao, C. Nie, H. Li, J. Shi, X. Liu, J. Jiang, S. Zuo, RSC Adv. **10**, 16749 (2020)
19.   S.T. Lee, M.J. Kim, G.G. Lee, S.G. Kim, S. Lee, W.S. Seo, Y.S. Lim, Curr. Appl. Phys. **17**, 732 (2017)
20.   A. Zatirostami, Thin Solid Films **725**, 138642 (2021)
21.   S.H. Chaki, M.D. Chaudhary, M.P. Deshpande, Mater. Res. Bull. **63**, 173 (2015)
22.   M. Liu, J. Zhang, J. Xu, B. Hu, K. Sun, Y. Yang, J. Wang, B. Du, H. Zhang, J. Mater. Chem. C **8**, 6422 (2020)
23.   F. Liu, P. Parajuli, R. Rao, P.C. Wei, A. Karunarathne, S. Bhattacharya, R. Podila, J. He, B. Maruyama, G. Priyadarshan, J.R. Gladden, Y.Y. Chen, A.M. Rao, Phys. Rev. B **98**, 224309 (2018)
24.   M.R. Pallavolu, S.K. Vishwanath, S.W. Joo, Mater. Lett. **281**, 128714 (2020)
25.   O. Madelung, in *Springer, Berlin, Heidelb.* (2004), pp. 556–605.
26.   Q. Chen, S. Bernardi, and Y. Zhang, ArXiv 1 (2017).
27.   P. Kumar, P. Sarkar, R.S. Katiyar, Opt. Mater. **133**, 112792 (2022)
28.   G. Jeong, J. Kim, O. Gunawan, S.R. Pae, S.H. Kim, J.Y. Song, Y.S. Lee, B. Shin, J. Alloys Compd. **722**, 474 (2017)
29.   P. Kumar, P. Sarkar, S. Singh, B.C.K. Mishra, R.S. Katiyar, Appl. Phys. A Mater. Sci. Process. **128**, 372 (2022)
30.   K. Assili, O. Gonzalez, K. Alouani, X. Vilanova, Arab. J. Chem. **13**, 1229 (2020)
31.   S. Gowthamaraju, U.P. Deshpande, P.A. Bhobe, J. Mater. Sci. Mater. Electron. **32**, 11781 (2021)
32.   C.C. Huang, Y.J. Lin, C.Y. Chuang, C.J. Liu, Y.W. Yang, J. Alloys Compd. **553**, 208 (2013)

33. J. Gainza, F. Serrano-Sánchez, J.E.F.S. Rodrigues, Y. Huttel, O.J. Dura, M.M. Koza, M.T. Fernández-Díaz, J.J. Meléndez, B.G. Márkus, F. Simon, J.L. Martínez, J.A. Alonso, N.M. Nemes, Cell Rep. Phys. Sci. **1**, 100263 (2020)